



Effect of dopant concentration on femtosecond pulsed laser irradiation of yttria-stabilized zirconia for generating nanopores

Yuka Yamamuro^a, Tomotaka Shimoyama^b, Hiroya Nagata^b, Jiwang Yan^{a,*}

^a Department of Mechanical Engineering, Faculty of Science and Technology, Keio University, Hiyoshi 3-14-1, Kohoku-ku, Yokohama 223-8522, Japan

^b Inorganic Materials Research Laboratory, TOSOH Corporation, Hayakawa 2743-1, Ayase 252-1123, Japan

ARTICLE INFO

Keywords:

Laser processing
Nanofabrications
Ceramics
Crystal structure
Light absorption and reflection
Oxide materials

ABSTRACT

Yttria-stabilized zirconia (YSZ) is a fine ceramics material that has been applied to dental implants and mechanical components. As YSZ is a hard, brittle, and chemically stable material, that undergoes phase transformation during mechanical loading, it is difficult to fabricate nanostructures using mechanical processing methods. In this study, a surface structuring method using a femtosecond pulsed laser was proposed, which is effective in suppressing the mechanical loading-induced phase transformation. As the material properties of YSZ vary with the concentration of yttria dopant, polycrystalline zirconia samples with different yttria concentrations (2, 3, 5, and 8 mol%) were used to investigate the effect of yttria concentrations on laser processing characteristics for nanostructuring. At all concentrations, nanopore generation in the surface grain was achieved by laser irradiation near the ablation threshold. In addition, there was no significant change in the crystal structure before and after laser irradiation, and no damage to the bulk occurred. At 2 mol%, intergranular cracks were generated around the pores. By increasing the dopant level to 5 mol%, the lens effect of the crystal grains became stronger due to enhanced grain growth, and the diameter and number of pores increased. In addition, pores formed preferentially on smaller grains at 5 mol%. However, for YSZ with 8 mol%, the pore formation phenomenon was different from that in the lower dopant level, as the area near the grain boundary was preferentially ablated, and microcracks formation and exfoliation of the surface also occurred. These results contribute to a deeper understanding of the laser ablation characteristics of zirconia with different dopant levels and to the development of surface structuring methods for fine ceramics materials.

1. Introduction

Zirconia-based ceramics have excellent material properties such as low thermal conductivity, heat resistance, high hardness, and chemical stability. Pure zirconia is usually stable at room temperature in a monoclinic crystal structure. However, as temperature increases, the monoclinic phase undergoes phase transformation, forming tetragonal and cubic phases, which induces a volume change, e.g., a 4% volume shrinkage in the monoclinic-tetragonal phase transformation. Since this temperature-induced volume change leads to material degradation, a small amount of metal oxide is generally added as a dopant to zirconia for stabilization of the tetragonal and cubic phases at room temperature in order to suppress the volume change. In particular, yttria-stabilized zirconia (YSZ), zirconia doped with yttrium oxide, is an important fine ceramic material used in various fields.

YSZ exhibits several distinctive material properties, which vary

depending on the dopant concentration. This is because the crystalline structure and grain size of YSZ vary depending on the dopant concentrations, resulting in changes in mechanical and optical properties. For example, with a small amount of dopant, the material becomes a partially stabilized YSZ with a slightly monoclinic phase in the tetragonal phase at room temperature, resulting in very high strength and high fracture toughness [1]. This is the effect of the stress-induced phase transformation mechanism. When small cracks occur on the surface, stress loading causes a local tetragonal-monoclinic phase transformation with volume expansion, resulting in the compressive stress on the crack tip inhibiting its propagation [1]. In particular, YSZ with 3 mol% yttria is used not only for biomaterials such as dental implant materials and artificial bones due to its special mechanical material properties and unique aesthetic effects, but also for various mechanical and electrical parts [2]. On the other hand, the more dopants around 8–10 mol%, the more oxygen vacancies are formed inside the YSZ crystal, resulting in

* Corresponding author.

E-mail address: yan@mech.keio.ac.jp (J. Yan).

<https://doi.org/10.1016/j.jalcom.2024.173596>

Received 14 October 2023; Received in revised form 28 December 2023; Accepted 18 January 2024

Available online 20 January 2024

0925-8388/© 2024 Elsevier B.V. All rights reserved.

excellent oxygen ion conductivity [3]. Taking advantage of this property, YSZ is attracting attention as a material for solid oxide fuel cells. Highly doped YSZ is also used in decorative applications because of its permeability. In summary, YSZ with different dopant concentrations exhibits diverse characteristics and thus can be used in a variety of applications.

Surface micro/nanostructuring can enhance and improve the surface functionality of products such as wettability, optical properties, biocompatibility, and friction coefficients, and is becoming increasingly important to enhance the value of materials and applications. For example, by forming micro/nanoscale parallel grooves and pyramid structures, surface wettability can be controlled from superhydrophilic to superhydrophobic, which is effective in antireflection and antifouling properties [4]. These micro/nanoscale patterns are also effective in controlling cell extensibility [5], improving adhesion to other materials [6], and improving friction properties [7]. Focusing on the application for biomaterial, Salou et al. [8] reported similar or higher osseointegration on nanostructured surfaces than on microstructured surfaces for dental implant application. In addition, nanoporous surfaces can also be expected to improve the adsorption of substances [9] and act as a carrier for different materials such as drug delivery systems [10] due to the increased surface area. Thus, micro/nanostructures bring about significant functional changes to material surfaces, and especially technology to generate nanoscale surface structures is necessary to enhance the surface functionality of zirconia products.

These patterned structures are processed in various ways depending on the target material and shape. There are many approaches to YSZ processing, however, they are difficult to generate nanostructures due to its unique material properties. For example, cutting and grinding are not suitable for fabricating nanoscale patterns because YSZ is hard and brittle. Sandblasting is conventionally used to make nanoscale roughed surfaces, it can induce phase transformation due to extreme mechanical reaction on the surface [11]. This phase transformation from tetragonal phase to monoclinic phase by stress loading during certain machining processes is a phenomenon unique to YSZ and is an issue that should be avoided during the process because it decreases the material strength and life [12]. Chemical treatments are not efficient due to its chemical stability [13]. In addition, surface patterning by thermal laser process has been reported due to its advantages of being a non-contact process and independent of the material hardness. However, it is limited to processing microstructures, and the formation of thick molten layers and cracks due to thermal stresses has been observed [14,15].

Thus, micro/nanofabrication using an ultrashort pulsed laser is regarded as an effective method for YSZ, because it can suppress thermal effects, which induce damage to the bulk causing material degradation, and allows localized processing. Many studies have reported microstructuring by ultrashort laser pulse irradiation on zirconia. Delgado-Ruiz et al. [16] fabricated microgrooves and micropore structures on the surface of dental zirconia. They showed that a precise, minimally damaging ultrashort pulsed laser is an interesting alternative to conventional zirconia microfabrication methods. Stanciu et al. [17] fabricated micropits with micrometric precise and defined edges and succeeded in creating multi-patterned YSZ. The authors also achieved precise micropyramid structure patterning by combining micro V-shaped grooves [18]. However, there have been few reports on nanostructures, especially nanoporous structures, except nanoscale structures known as laser-induced periodic surface structures (LIPSS) [19], as per the author's best knowledge.

In our previous study, we proposed a novel method for generating nanopores in the YSZ surface using femtosecond pulsed lasers [20]. By irradiating YSZ with 3 mol% yttria with laser pulses at very low power, numerous pores with depths of several hundred nanometers could be fabricated in the surface grains. However, the polycrystalline YSZ with different yttria concentrations have different crystal structures, resulting in changes in grain size, optical properties such as refractive index, and thermal conductivity, which affect the interaction of laser beam and

material during laser processing. For example, Heiroth et al. [21] investigated ablation characteristics in the pulsed laser deposition (PLD) process and revealed the ablation phenomena were significantly different between YSZ with 3 mol% and 9.5 mol% yttria. However, this experimental condition is different from the phenomena that occur during nanopore generation at very low laser power. Cui et al. [22] performed femtosecond pulsed laser irradiation to fabricate ultra-sharp V-notch on 3Y-TZP and 8Y-FSZ. They mainly focused on the strength evaluation of the material but did not have enough discussion about the ablation characteristics of each sample. Up to date, the femtosecond pulsed laser nanofabrication characteristics of zirconia with different yttria concentrations still remain unclear.

In this study, polycrystalline zirconia with different yttria concentrations were used to investigate the effect of yttria concentration on laser processing characteristics during nanofabrication by femtosecond pulsed laser irradiation. Differences in fundamental characteristics of nanopore formation of each sample were explained by differences in intragrain light focusing effects due to the crystal structure and grain morphology. Furthermore, the laser-induced change in the crystal structure of YSZ was evaluated. This study aims to deepen understanding of the phenomena of nanopores generation in YSZ, and thus provide an approach for various fields in the industry to enhance surface functionality.

2. Experiments

An Yb: KGW laser (PHAROS-08-600-PP, Light Conversion, UAB, Lithuania) was used in this study. It has a laser wavelength of 1028 nm, a pulse width of 256 fs, and a repetition frequency of 100 kHz. The laser beam had a Gaussian energy distribution and was linearly polarized. A Schematic of the optical system is shown in Fig. 1. The scanning of the laser beam was controlled in the X- and Y-axis by a galvanometer scanner system, and WinLase Professional software was used to create laser motion programs. The laser beam was focused onto the workpiece surface on the precision stage by an f θ lens. The focal length was approximately 70 mm, and the laser spot diameter was adjusted to 16–20 μ m at the focal point. After the laser power was controlled with the laser oscillator and the attenuator, the laser beam was scanned in a line in the air. Table 1 summarizes the experimental parameters. For nanopore generation, the parameters were set according to our previous study [20]. To minimize the thermal effect during the laser process, the minimum pulse width (256 fs) of the laser system was used. The laser power was varied in a wide range with 50 mW increments to be near the ablation threshold of zirconia as it is highly dependent on nanopore formation. In this study, the scanning speed was set to 1000 mm/s (the pulse overlap rate of \sim 0%) to make the interval distance between adjacent irradiated pulses onto the sample wider to generate nanopore clear and avoid the removal of the top layer.

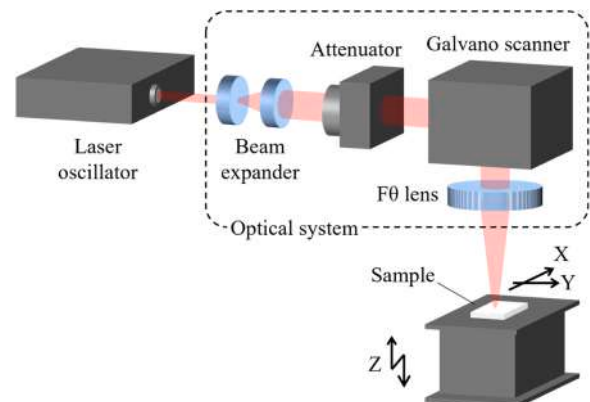


Fig. 1. Experimental setup of laser optical system.

Table 1
Experimental conditions.

Laser medium	Yb: KGW
Wavelength [nm]	1028
Spot size [μm]	16 - 20
Pulse width [fs]	256
Repetition frequency: f [kHz]	100
Scanning speed: v [mm/s]	1000
Laser power: E [mW]	200 - 600
Laser fluence: F [J/cm^2]	1.0 - 3.0
Number of scans: N	1
Atmosphere	Air

Fully sintered YSZ polycrystalline containing 2 mol% (2Y), 3 mol% (3Y), 5 mol% (5Y), and 8 mol% (8Y) Y_2O_3 (Tosoh Corp., Japan) was used as workpieces. 2Y, 3Y, 5Y, and 8Y were manufactured by sintered at 1450 °C, 1300 °C, 1450 °C, and 1350 °C for 2 h, at a constant heating rate of 100 °C/h, respectively. The sintered samples were rectangular-shaped plates with dimensions of 10–20 mm \times 10–20 mm \times 2–3 mm. Since nanopore formation is highly dependent on the surface grain shape and is formed by the light-focusing effect within the grains due to the convex shape of the grains [20], unpolished samples were used. All samples were cleaned with ethanol and acetone and dried with air spray before laser irradiation.

The average grain size of the sample was measured by the planimetric method [23], and the surface roughness was measured by a laser probe profilometer (MP-3, Mitaka Kohki Co., Ltd, Japan). An atomic force microscope (AFM, SPM-3, Hitachi High-Tech Corp., Japan) was used to measure the three-dimensional surface topography of the sample. The optical properties of the sample were measured by a UV–visible–NIR spectrophotometer (UV-3600 Plus, Shimadzu Corp., Japan).

After the irradiating laser, the surface morphologies of the samples were observed using a field-emission scanning electron microscope (FE-SEM, Inspect F50, FEI Co., USA). To investigate the cross-sections of the samples, the sample was cut by a focused ion beam (FIB) system. To identify the material defects, a cross-section of the sample was observed using an FE-SEM (ZEISS GeminiSEM 500, Carl Zeiss AG, Germany), equipped with an electron backscatter diffraction (EBSD) detector (EDAX Inc., USA). Then a transmission electron microscope (TEM, Tecnai Osiris, FEI Co., USA) was used to observe the cross-sections. To evaluate the crystal phase in the subsurface region, selected area electron diffraction (SAED) was used. Mapping analysis with energy-dispersive X-ray spectroscopy (EDX) was used to clarify the distribution of the yttria dopant.

For quantitative analysis, pore size was calculated by image analysis of the irradiated area. The brightness of the SEM images was binarized by setting the threshold value using ImageJ software. The pores were extracted from the images and then the pore size was calculated. For the calculation, six SEM images of laser irradiated area with a size of 10 μm \times 10 μm were used for each sample.

For the evaluation of the material phase structure, a laser micro-Raman spectrometer (InVia Raman Microscope, Renishaw plc., UK), with a laser wavelength of 532 nm and a beam diameter of 1 μm , suitable for local measurement, was used in a laser ablated region. For crystallographic analysis of the bulk before laser ablation, an X-ray diffraction (XRD) system (D8 Discover, Bruker Corp., USA), was used for the original YSZ surface. For the evaluation of the mechanical properties of the YSZ after laser irradiation, a three-point bending test was conducted under the JIS R1601 standard. The test was conducted five times under each condition, and the average value was obtained.

3. Results and discussion

3.1. Pore morphology characterization

For the comparison of the nanopore generation phenomena of each YSZ sample, line irradiation was carried out near the ablation threshold. First, the irradiated surfaces of each sample were compared when irradiated at the same laser power. Fig. 2 shows the SEM images of the irradiated surface with a laser power of 350 mW. The low-magnification images (Fig. 2(a1)–(d1)) show that the surface was processed for each pulse because there was almost no overlap between each pulse due to the high-speed beam scanning. In 2Y~5Y, the nanoscale pores formed at irradiated area, however, in 5Y, the distribution of pores was different for each irradiated area. In 8Y, the surface was processed unevenly.

From high-magnification images (Fig. 2(a2)–(d2)), in 2Y, pores formed uniformly within a circular region, and numerous intergranular cracks were also observed around the pores, regardless of whether they were in the center or the periphery of the circular region. In 3Y, a few intergranular cracks were observed. Pores uniformly formed within the circular region, and the pore diameter tended to decrease toward the outside, away from the center region due to the Gaussian energy distribution of the laser beam. In 5Y, pores were preferentially formed on small grains, and relatively large grains at the center of the spot with the highest energy were hardly processed. In addition, it was found that some pores formed near the grain boundaries of larger grains. In 8Y, the center of the spot was completely ablated, and the surface layer was removed. Microcracks and small pores were observed in the irradiated area. For further investigation of the irradiated surface of 8Y, magnified SEM images featuring two different spots irradiated at 350 mW are shown in Fig. 3. In Fig. 3(a), where the laser pulse was irradiated to the 8Y grain boundary gathering area, the YSZ surface was not completely ablated and the surface layer remained. There were large microcracks and partial surface delamination near the grain boundaries. On the other hand, in Fig. 3(b), where the laser pulse was irradiated to the center of the surface grain, most of the surface layer was removed. The surrounding grains adjacent to the ablation-detached grain had continuous elongated pores and cracks along the grain boundaries. On both irradiated surfaces, multiple very small shallow pores formed on the grains. According to these results, it was found that pores form in each YSZ with any of the four dopant levels, but their surface morphology is distinctly different. Therefore, the changes in surface morphologies with laser power were investigated in detail for each YSZ sample.

Fig. 4 shows the SEM images of the irradiated surface of 2Y with varying laser power. The processed area increased with increasing power. At 300 mW, few pores sparsely formed on the surface grains. Many grain boundary spallation, i.e. intergranular cracks, was also found in the irradiated region. By increasing the laser power to 400 mW, pores were processed uniformly at all locations. The number of pores and intergranular cracks increased, and a molten area was observed at the center of the irradiated area. Over 500 mW, the original surface layer was almost gone, and a molten surface was formed by ablation. However, intergranular cracks were still uniformly present outside of the irradiated area.

Fig. 5 shows the SEM images of the irradiated surface of 3Y. At 300 mW, pores were generated non-uniformly, but as in the case of 2Y, the number of pores formed in the surface grains increased with increasing power, and pores formed uniformly within the irradiated area. At 400 mW, adjacent pores were connected and elongated pores were formed. Over 500 mW, the center of the pulse was ablated entirely, creating a molten surface. At all powers, the number of intergranular cracks was very small compared to 2Y.

Fig. 6 shows the SEM images of the irradiated surface of 5Y. At low power (300 mW and 400 mW), pores were partially formed and did not correspond to the circular shape of the pulse. The number of pores increased as the power increased, but pores preferentially formed on smaller grains and were randomly arranged to avoid larger grains in the

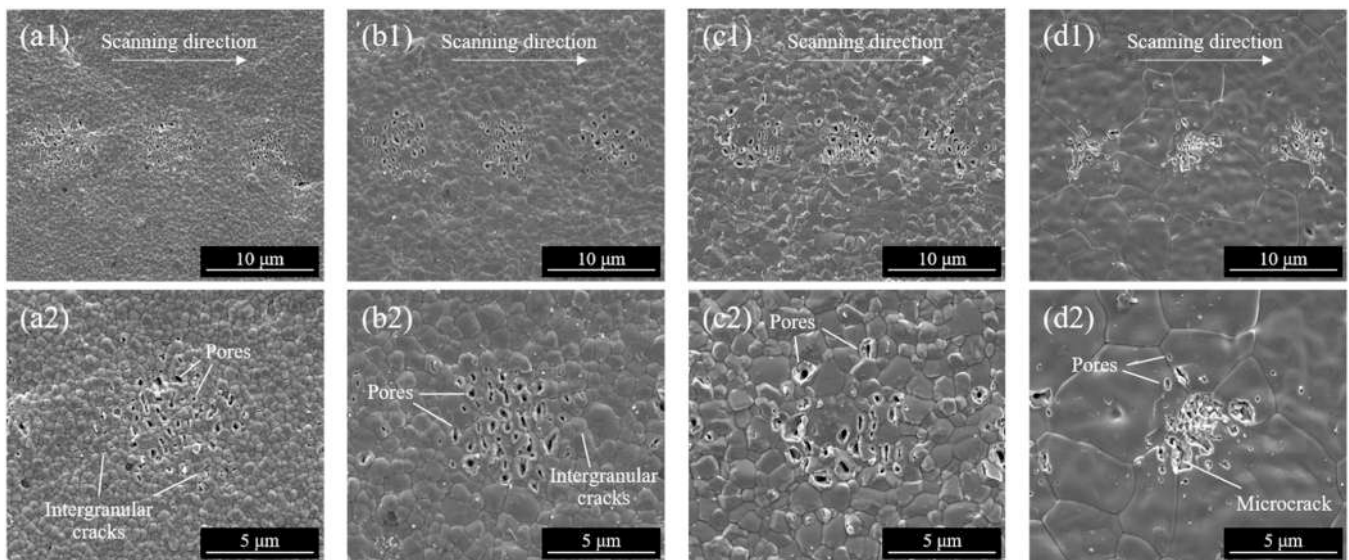


Fig. 2. SEM images of irradiated surface: (a) 2Y, (b) 3Y, (c) 5Y, (d) 8Y. (a1)–(d1) are low-magnification images, and (a2)–(d2) are high-magnification images.

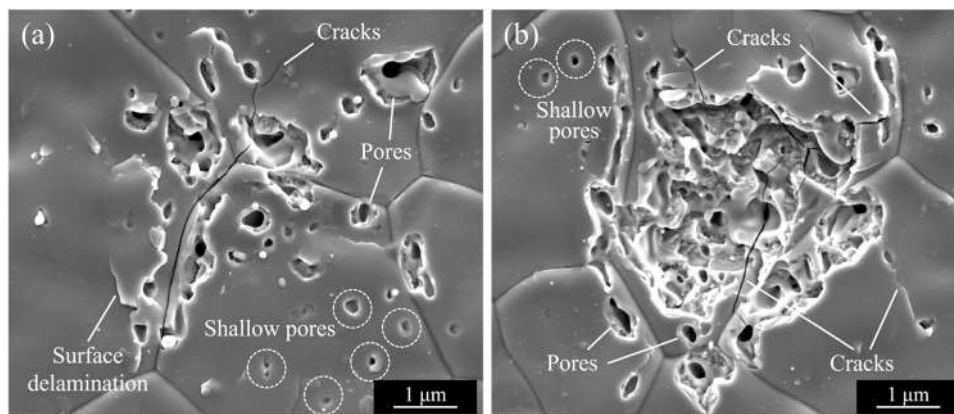


Fig. 3. Magnified SEM images of 8Y irradiated at a laser power of 350 mW, where laser pulse was irradiated at (a) region of a dense grain boundary, (b) center of the surface grain.

irradiated area. Compared to the pores generated in the 3Y surface, the pore aperture edges were sharper. At 500 mW, the center of the pulse was processed regardless of the size of the grains. 600 mW showed multiple microcracks in the machined area.

Fig. 7 shows the SEM images of the irradiated surface of 8Y. At 300 mW, small pores were concentrated near the grain boundaries. At 400 mW and above, the surface layer was completely removed and individual pores were not discernible. The irradiated area was uniformly machined and cracks were observed. The removed area increased with increasing the power, and small shallow pores also formed on the surrounding grains. At 600 mW, large microcracks extended over the grains regardless of the grain boundaries in both irradiated and unirradiated areas. Fig. 8 shows the AFM surface images of YSZ irradiated at 400 mW. The three-dimensional topography shows that the surface topography, including the curvature, is significantly different between the grains with and without pores in 5Y (Fig. 8(a)). In contrast, in 8Y (Fig. 8(b)), where the surface layer was removed, there were some grain surface irregularities over the entire area. In 2Y, 3Y, and 5Y, many pores were observed on the machined surface even at high ablation power, while in 8Y, uneven surfaces were formed on the entire ablated area.

To investigate the unique processing characteristics of 8Y in detail, an EBSD analysis of the cross-section was performed. The cross-sectional images of 8Y irradiated at 400 mW are shown in Fig. 9. From the image

quality (IQ) map (Fig. 9(a)), it was found that there were many dark dots, corresponding to residual pores inside the grains. The inverse pole figure (IPF) map and kernel average misorientation (KAM) map clarified grain boundaries and revealed that there was a high density of strain inside the grains near the surface layer of the laser-irradiated area (Fig. 9 (b), (c)). The strain extended to a depth of several micrometers inside the grains, which may be attributed to microcracks observed in Fig. 9. Cross-sectional observations of nanopores fabricated in 3Y surfaces in previous studies did not show such internal defects [20], suggest that different dopant concentrations cause different processing phenomena.

3.2. Pore size analysis

For quantitative analysis, the diameters of the individual pores irradiated in YSZ samples with different yttria concentrations were calculated. The distribution of pore diameters for 2Y, 3Y, and 5Y, the conditions under which clear pore formation was observed, is shown in Fig. 10. To distinguish between pores generated by laser irradiation from and residual pores originally generated during the sintering process of the ceramics, a diameter of 50 nm was used as cutoff diameters for all dopant concentration. As the dopant concentration increased from 2 mol% to 5 mol%, the diameter shifted gradually to larger values. In 2Y, no pores were generated in the range of above 160 nm under this

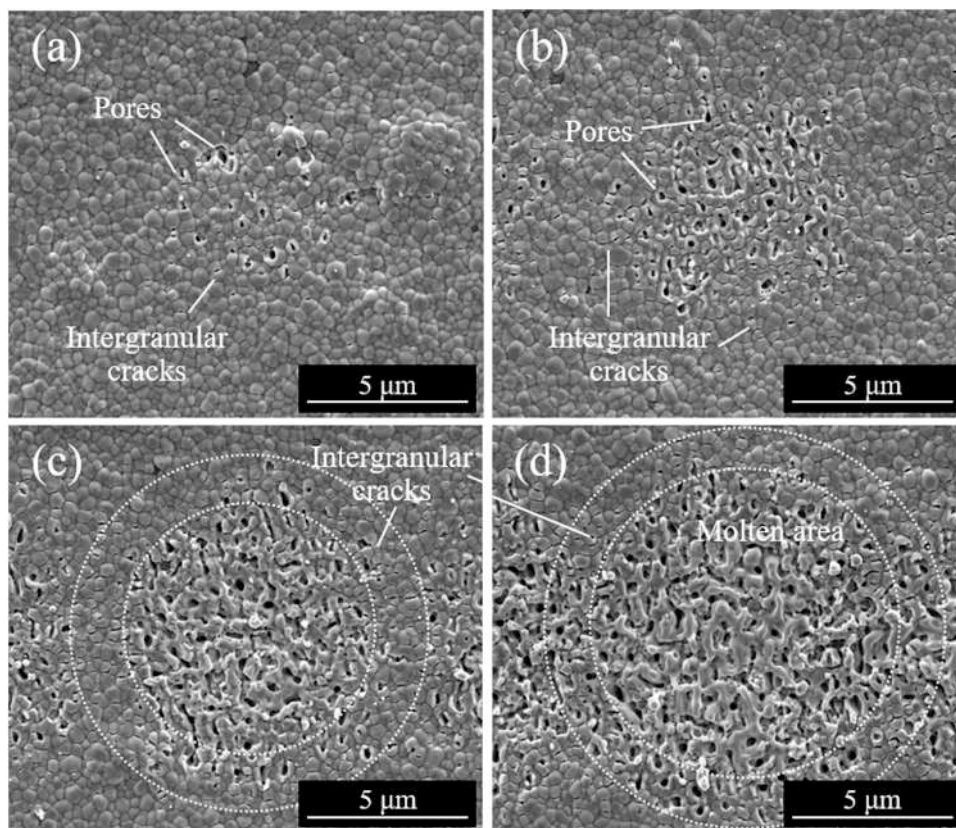


Fig. 4. SEM images of the irradiated surface of 2Y with varying laser power: (a) 300 mW, (b) 400 mW, (c) 500 mW, (d) 600 mW.

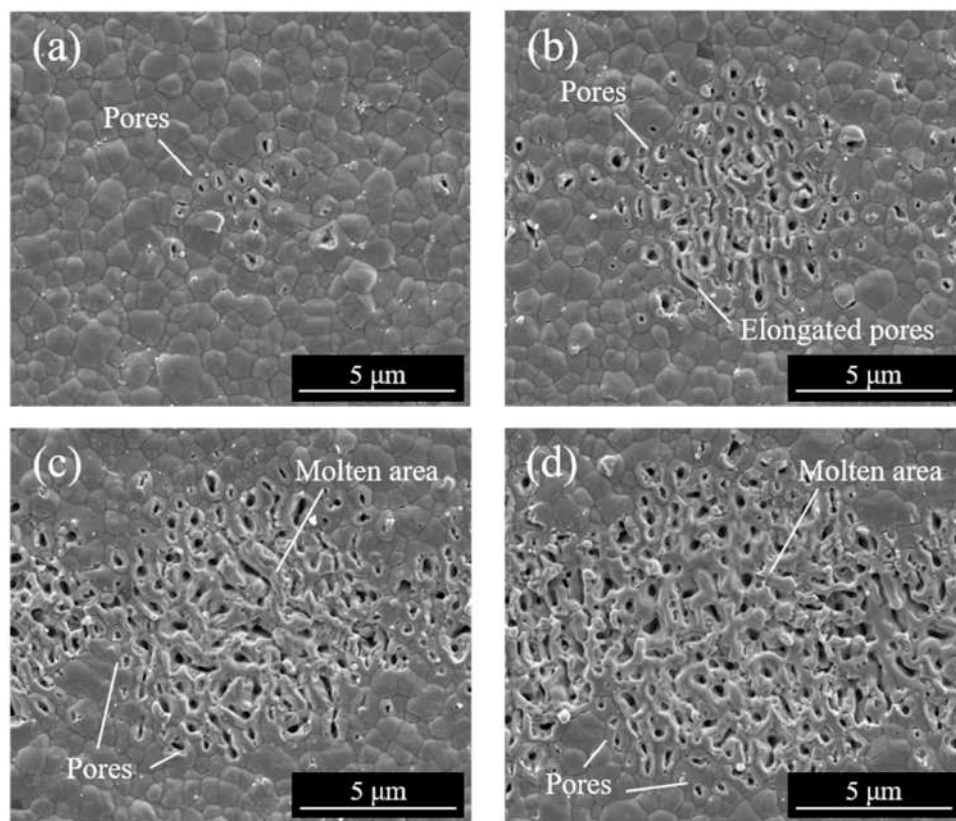


Fig. 5. SEM images of the irradiated surface of 3Y with varying laser power: (a) 300 mW, (b) 400 mW, (c) 500 mW, (d) 600 mW.

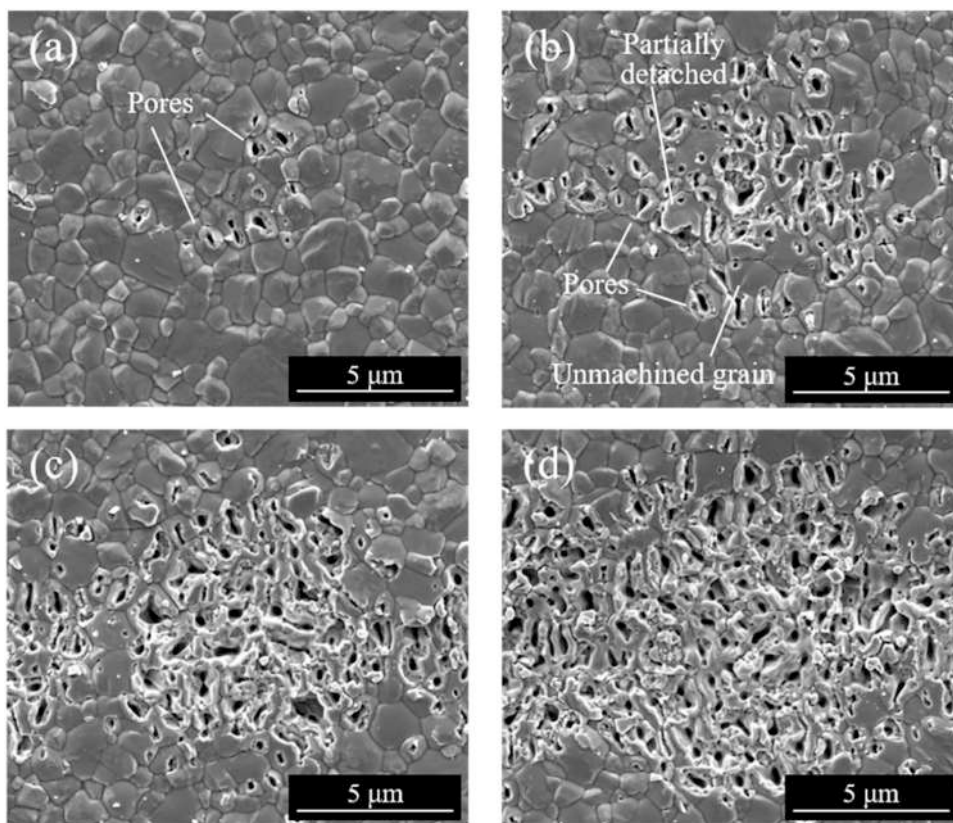


Fig. 6. SEM images of the irradiated surface of 5Y with varying laser power: (a) 300 mW, (b) 400 mW, (c) 500 mW, (d) 600 mW.

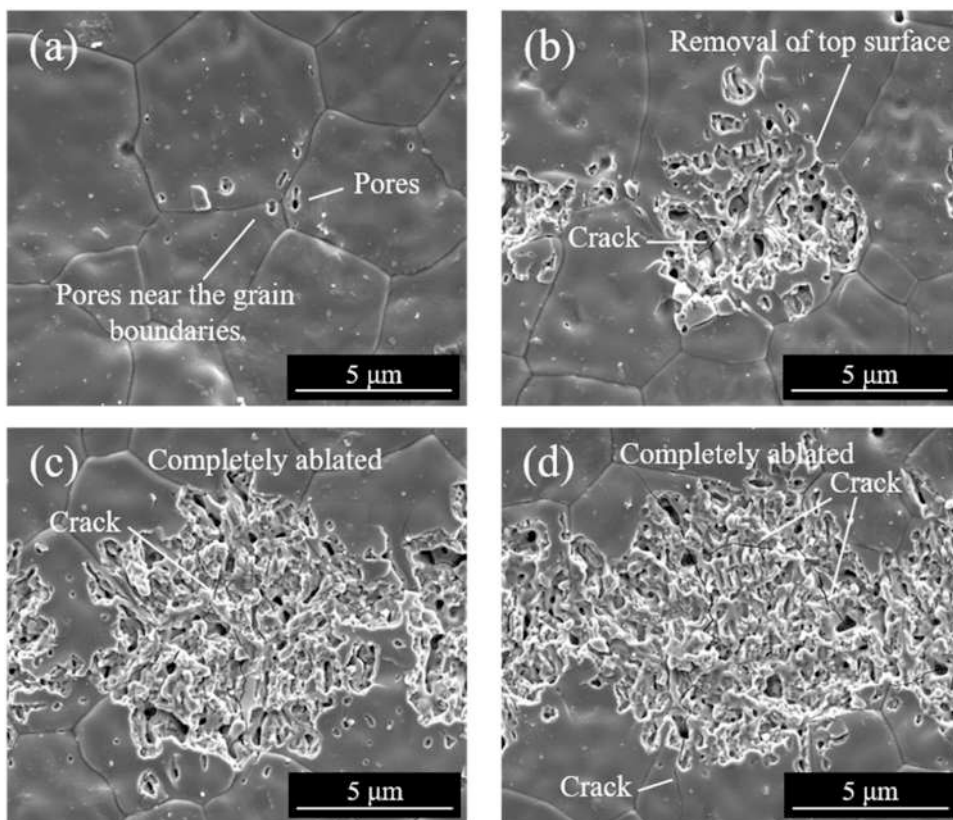


Fig. 7. SEM images of the irradiated surface of 8Y with varying laser power: (a) 300 mW, (b) 400 mW, (c) 500 mW, (d) 600 mW.

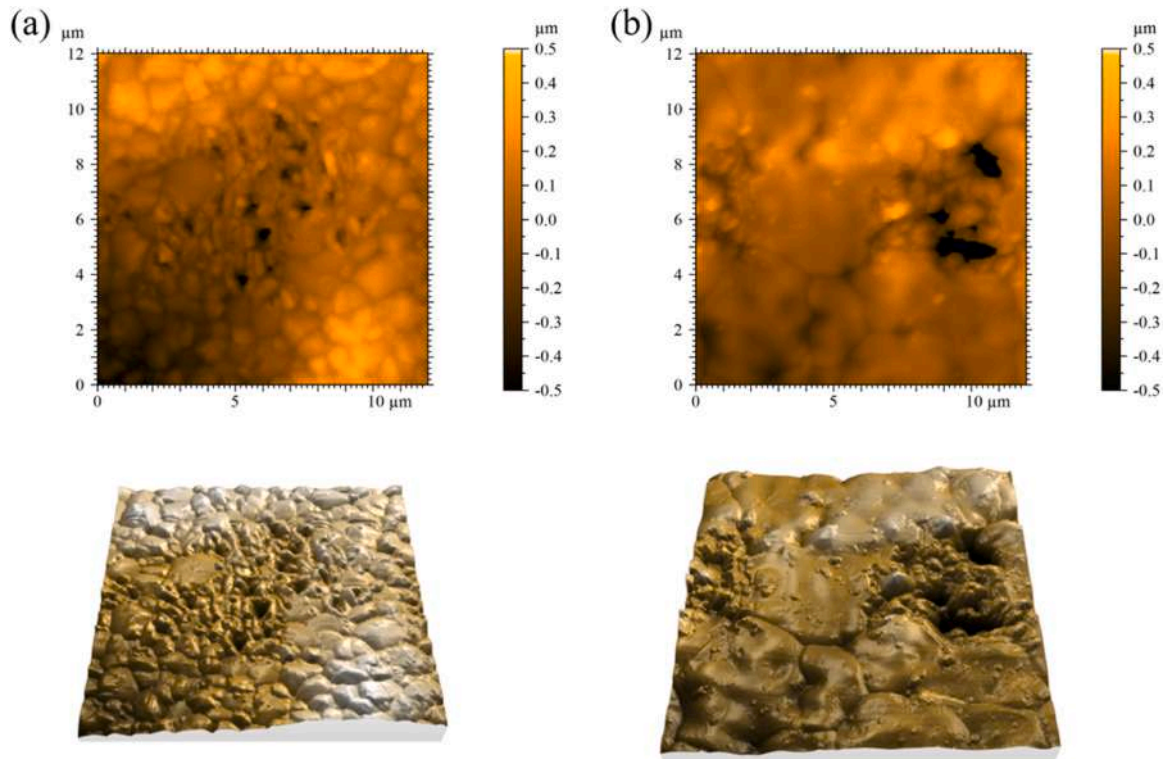


Fig. 8. Surface topography of irradiated area: (a) 5Y, (b) 8Y.

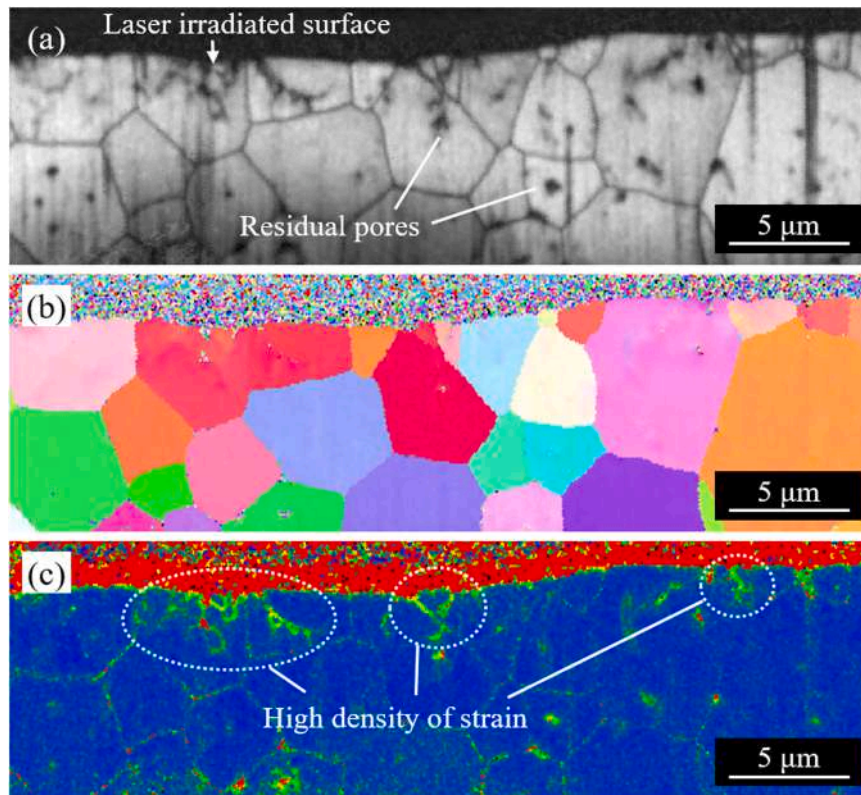


Fig. 9. Cross-sectional images of the irradiated 8Y surface at a laser power of 400 mW: (a) IQ map, (b) IPF map, (c) KAM map.

condition. On the other hand, in 5Y, pore size was distributed in the entire range of 60–200 nm and there were some pores with diameter values over 200 nm. In addition, the sample with higher concentrations

(3Y and 5Y) showed a significantly larger number of pores than those with lower concentrations (2Y). Even in 3Y and 5Y, there was a distribution of pores on the small values with diameters of under 100 nm.

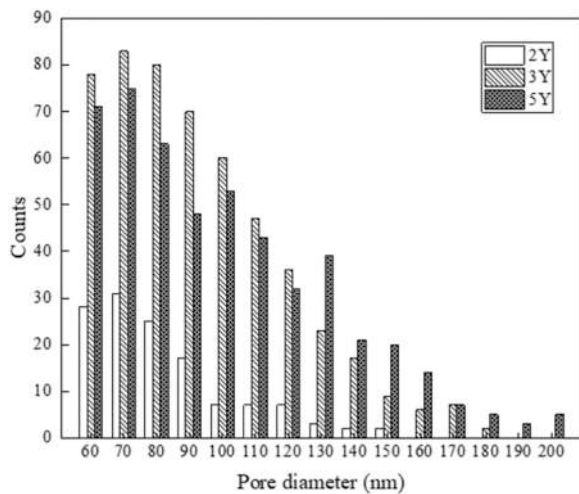


Fig. 10. Change in pore diameter of YSZ with different dopant concentrations.

This is because the laser beam has a Gaussian energy distribution, and in the region where the outer edge of the laser spot with low energy is irradiated, there is less absorption and the amount of material removal decreases. The pore diameter also increased with increasing yttria concentration, clearly indicating that there is a difference in the interaction between the laser beam and the material. A detailed discussion of this phenomenon will be given in Section 3.6.

3.3. Pore cross-sectional observation

To investigate the subsurface structural change in detail, cross-sectional observation was performed for four different YSZ samples. Fig. 11 shows TEM images of pores generated by laser irradiation and SAED patterns measured around the wall of the pore, i.e., the processed area, and at a distance from the processed area within the same grain. In all samples, pores were formed within the zirconia grains. However, it cannot be said that the entire pore was necessarily cut out by FIB this time. In a previous study, a pore with a depth of about 500 nm was formed in 3Y [20]. Thus, there is a great possibility that these pores presented in Fig. 11 are a partial cross-section of a pore and that the pore is much deeper. In 2Y, a perfectly regular crystal pattern was not obtained at the pore wall area. This indicates the presence of a molten surface due to localized ablation and outward ejection of material within the grain during the nanopore generation process. On the other hand, a clear tetragonal SAED pattern was detected immediately adjacent to the pore. This indicates that the pore formation occurred locally within a single grain and that most of the crystalline structure within the grain was unaffected by the laser processing and was well preserved. A more regular SAED pattern was detected at the 3Y pore wall than at the 2Y pore wall. This was almost the same crystalline pattern as that obtained in the area away from the pore within the same grain, and this pattern indicated tetragonal crystals. In this sample, it was found that thermal effects with melting did not occur until just at the ablation boundary of the pore. For 5Y and 8Y, the same strong SAED pattern indicating cubic crystal was detected at the pore wall and in the region away from the pore, respectively. It was found that there was little or no formation of a molten layer at the ablation boundary of the pore wall and that there was no change in the crystal structure inside the surface grains due to laser irradiation for YSZ with any dopant concentration.

Fig. 12 shows elemental mapping images of the cross-sections of the pores. In all YSZs, the distribution of zirconium (Zr) was uniformly present. As for yttrium (Y), no significant shading was observed in 2Y, while in 3Y, yttrium was concentrated at the grain boundaries along the contours of the pore-forming grain, indicating segregation at the grain boundaries. In 5Y, yttrium concentration in the pore-forming grain was

less than that in the adjacent grains. In 8Y, yttrium was uniformly distributed independent of grain boundaries.

3.4. Material phase analysis

To investigate the possibility of phase transformation during laser processing, the Raman spectra of the irradiated surface of YSZ with different dopant levels were measured. Fig. 13 shows the results of the sample surface irradiated at 600 mW. Tetragonal peaks at 147 cm^{-1} and 264 cm^{-1} were identified on the 2Y, 3Y, and 5Y surfaces, before and after laser irradiation. Between these tetragonal peaks, a slight increase in the spectrum was observed at 181 cm^{-1} and 190 cm^{-1} corresponding to the monoclinic peak. A peak shift around 640 cm^{-1} was observed in 5Y corresponding to an increase in the cubic phase, and in 8Y, only completely cubic peaks were observed. At all yttria concentrations, there was no change in Raman spectra before and after laser irradiation. This indicates that the laser-induced thermal effect is quite small and that phase transformation to a crystal structure such as a monoclinic does not occur, which is also consistent with the result of cross-sectional observation by TEM (Fig. 11).

In general, irradiating YSZ with a long-pulse laser causes thermal damage due to laser-induced tetragonal-monoclinic phase transformation due to temperature increase [14,24]. However, when femtosecond pulsed lasers are used, the pulse width is much shorter than the time it takes for heat transfer to occur, thus limiting the damage to the irradiated area. It was found that in microstructuring, the monoclinic phase originally present in the sample could be almost removed and did not induce further monoclinic phase growth in the material around the irradiated area during femtosecond pulsed laser ablation [16]. We also showed that the original monoclinic phase could be further reduced by appropriately varying the laser parameters [18]. For nanostructuring, however, there were still a few examples of phase transformation measurements.

In this nanoscale processing, a significant increase in the monoclinic peak was not observed after laser irradiation, and there was no phase transformation of not only the monoclinic but also the original crystal structure of YSZ. The results of this study indicate that regardless of the original crystal structure, corresponding to dopant concentrations, nanostructuring using low laser power with a femtosecond pulse does not cause phase transformation to the sample.

3.5. Material strength test

Material strength tests were conducted to investigate the change in material properties of YSZ after laser processing and to quantitatively analyze the lack of damage to the bulk of the nanopore-generated surface. Fig. 14 shows the change in bending strength measured before laser irradiating and at the nanopore-generated surface in 2Y, 3Y, and 5Y, the sample with uniformly formed pores, and 8Y. The strength of the original YSZ is greatest at 3Y, which is consistent with the fact that the stress-induced phase transformation strengthening mechanism is most effective at 3 mol%, and this effect is lost at higher concentrations, resulting in a decrease in strength. The strength of the pore-fabricated surfaces was slightly reduced in three samples (2Y, 3Y, and 5Y), but the difference was not significant based on the error range. On the other hand, 8Y showed a slight increase in strength after laser irradiation. Although microcracks were observed in the 8Y surface after laser irradiation, it is assumed that the strength increased due to the compressive stresses on the sample surface as shown in Fig. 9. This indicates that the nanopore generation method, which adds structure only to the surface layer of the material, is an effective method of surface nanostructuring without significantly affecting the reduction in the bending strength of the sample.

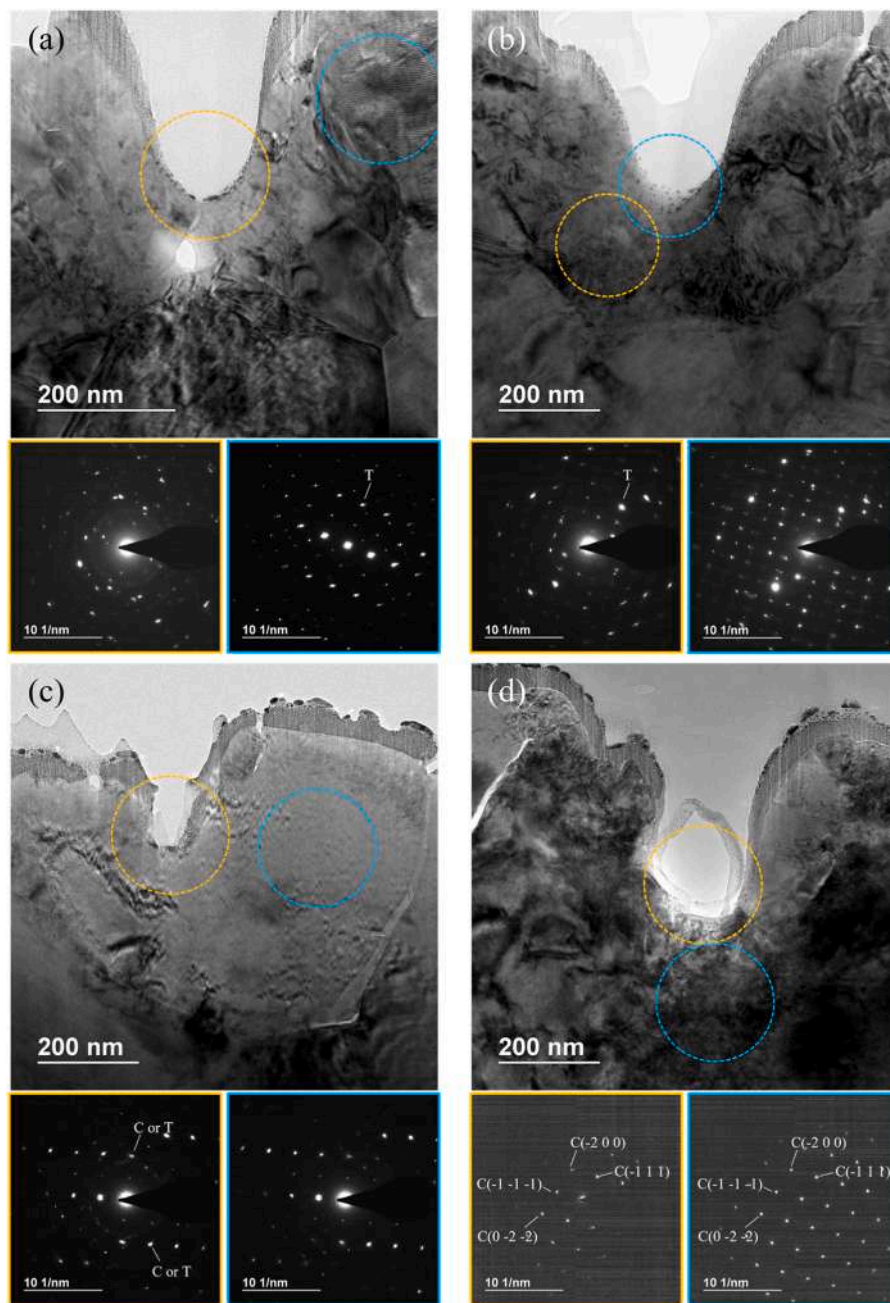


Fig. 11. TEM images and SAED patterns of the cross-section of YSZ irradiated at 400 mW: (a) 2Y, (b) 3Y, (c) 5Y, (d) 8Y. (T indicate tetragonal and C indicate cubic).

3.6. Mechanism of dopant effects on laser processing characteristics

Based on the results in previous sections, the processing characteristics of nanopores in YSZ with different dopant levels were revealed. Nanopores are considered to be formed when an incident beam at very low energy irradiated on surface grains passes into the interior of the grains due to the lens effect of the convex shape of the grain surface, resulting in a localized increase in energy and ablation within the grains. Since the YSZ polycrystalline surface is composed of highly permeable grains at the wavelengths of the experiment ($\lambda = 1028 \text{ nm}$), an increase in local energy intensity significantly increases absorption. Therefore, the surface grain shape and the behavior of the laser beam inside the material are considered to be important factors in the formation of pores.

For the detailed investigation, the topography of the exposed grains on the surface was measured, and the results are shown in Fig. 15. 2Y

and 3Y were relatively uniform in grain size, while 5Y was composed of small and large grains. Compared to the other samples, 8Y was composed of very large grains, and intra- and intergranular residual pores were noticeable on the surface. The measured average grain sizes of each sample were $0.47 \mu\text{m}$, $0.75 \mu\text{m}$, $1.18 \mu\text{m}$, and $5.13 \mu\text{m}$, respectively. The surface roughness of each sample is also summarized in Fig. 16. The surface roughness showed a decreasing trend with increasing dopant concentration, but the value increased and the range of error increased for 8Y, possibly since the surface of one of the grains was randomly bumpy in 8Y.

Then, the characteristics inside the material were investigated. Fig. 17 shows the EDX map of a cross-section of the original YSZ substrate. Yttrium (Y) distribution was identified by these images. yttrium accumulation was observed along the grain boundaries of 2Y, especially at the point where the three grains meet. 3Y showed an increased amount of grain boundary segregation compared to 2Y. In 5Y, yttrium

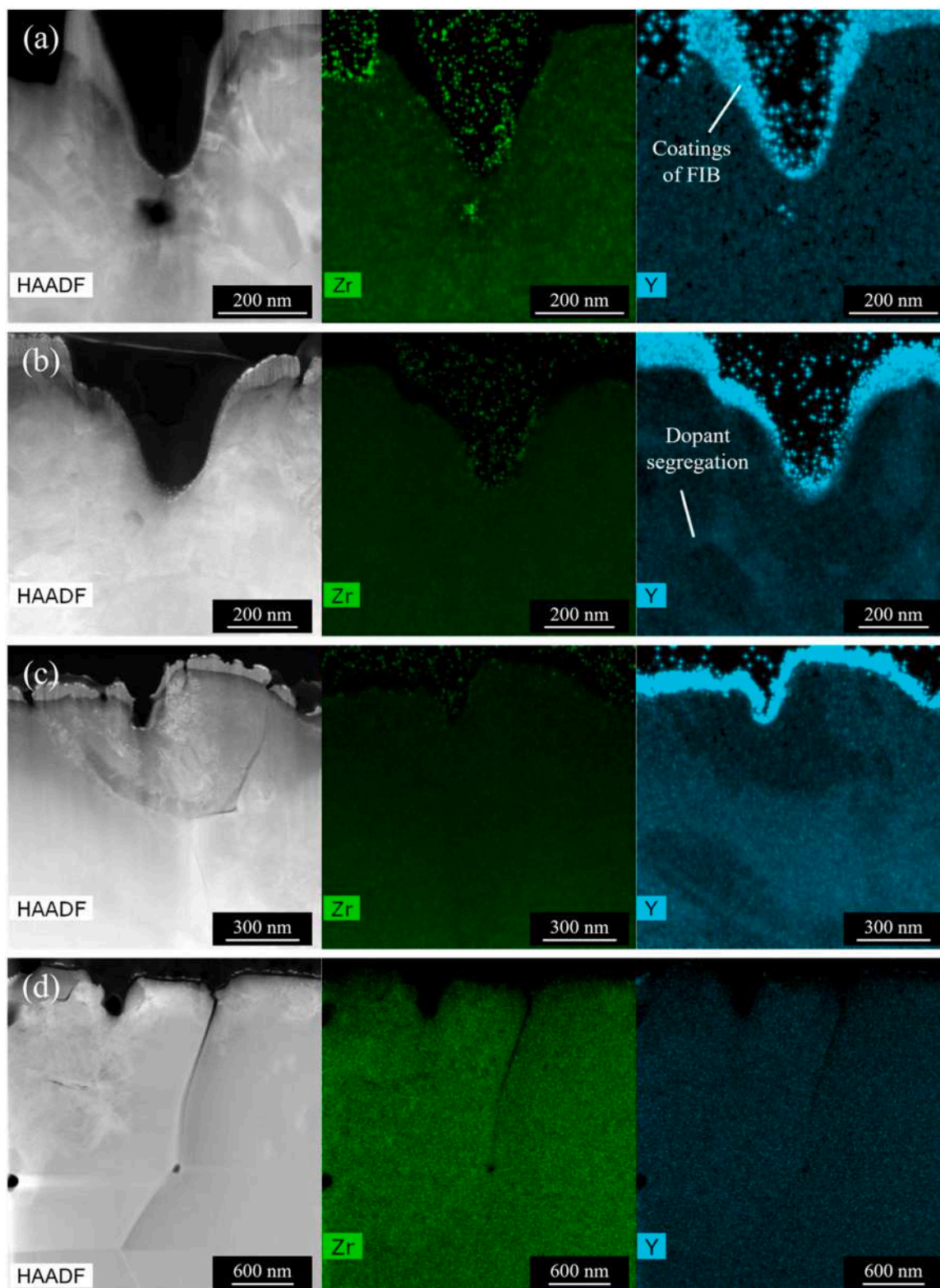


Fig. 12. Elemental mapping images of the cross-sections of the pores.: (a) 2Y, (b) 3Y, (c) 5Y, (d) 8Y. The green-colored area corresponds to Zr, and the blue-colored area is Y.

was uniformly distributed not only along grain boundaries but also within grains, and there were regions of dense and less yttrium within a single grain. In 8Y, yttrium was not accumulated at certain points, such as grain boundaries, and was uniformly distributed within the material. Since the crystal structure of YSZ generally changes with the dopant

level [25], the crystal structure of the YSZ substrate was investigated. Fig. 18 shows the XRD spectra of the original laser-unirradiated surface. 2Y and 3Y were mainly composed of tetragonal and slightly monoclinic phases. With increasing yttria concentration, the cubic peaks gradually increased, and monoclinic phases completely disappeared in 5Y. At

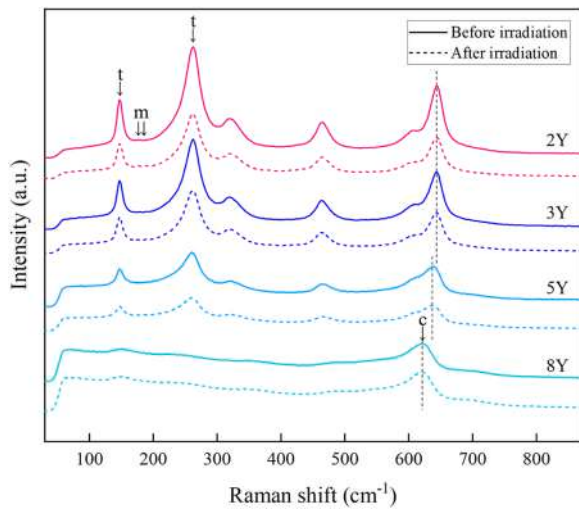


Fig. 13. Raman spectra of the before and after irradiated surface with different yttria concentrations.

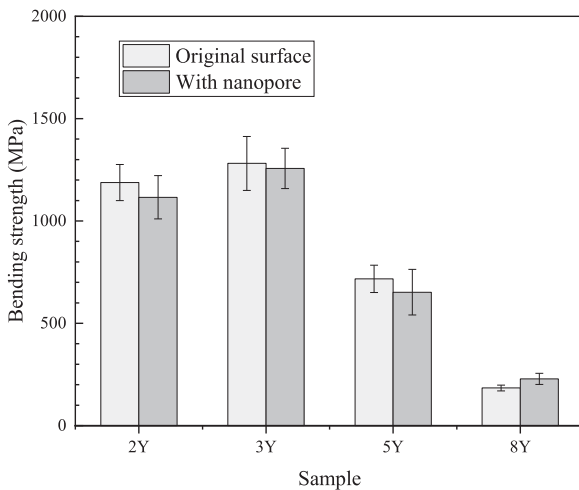


Fig. 14. Change in bending strength of YSZ before and after nanopore fabrication.

higher concentrations, 8Y was composed only of cubic phases. These results indicate that grains with high yttria concentration part correspond to grown large cubic crystals, while those with low yttria concentration and small grains correspond to tetragonal and monoclinic crystals.

Thus, YSZ polycrystals are composed of different crystal structures, and the behavior of light is expected to depend on them. Generally, light traveling inside polycrystalline ceramics is scattered by the following causes: (i) scattering due to residual pores formed inside the material during the sintering process, (ii) scattering due to segregation and precipitation of additives, (iii) scattering due to imperfections in the crystal structure such as point defects and dislocations at grain boundaries, and (iv) scattering at discontinuous interfaces such as grain boundaries due to the optical anisotropy of the crystal. First, the effect of the difference in crystal structure of zirconia on scattering was considered. In general, the real in-line transmission T of ceramics materials is given by the following equation [26]:

$$T = (1 - R)e^{-\gamma t} \quad (1)$$

where R is the surface reflectance, γ is the light attenuation coefficient, and t is the thickness of the sample, respectively. R is given as follows:

$$R = \frac{2R'}{1 + R'} \quad (2)$$

$$R' = \left(\frac{n-1}{n+1} \right)^2 \quad (3)$$

where n is the refractive index of the sample. For ceramics composed of a single crystal without impurities, γ corresponding to light scattering is calculated as the sum of the scattering at the grain boundary due to differences in refractive index (γ_g) and the scattering due to vacancies at the grain boundary (γ_v) [26,27]:

$$\gamma = \gamma_g + \gamma_v \quad (4)$$

$$\gamma_g = \frac{3\pi^2 d_g \Delta n_g^2}{\lambda^2} \quad (5)$$

$$\gamma_v = \frac{6p\pi^2 d_v \Delta n_v^2}{\lambda^2} \quad (6)$$

where λ is the light wavelength, p is the porosity, d_g is the diameter of grain, and d_v is the diameter of vacancy, respectively. In this study, γ_g was focused on considering the behavior of light at grain boundaries during laser processing. In Eq. (5), Δn_g is given as the difference between the maximum refractive index n_{max} of a crystal with birefringence and the average refractive index n_{ave} , as follows:

$$\Delta n_g = n_{max} - n_{ave} \quad (7)$$

Since cubic crystals, which mainly constitute YSZ with high dopant concentration, are optically isotropic crystals, $\Delta n_g = 0$ and $\gamma_g = 0$ from Eq. (5). Therefore, assuming no vacancies inside the ceramics, there is no scattering at the interface in the cubic crystal. On the other hand, tetragonal (and monoclinic) crystals within YSZ with low dopant concentration are anisotropic crystals, so Δn_g has a value and light attenuation occurs due to scattering inside the material. However, it should be considered that residual pores, yttria dopant segregation, and lattice defects at grain boundaries also cause scattering in the actual sample.

To discuss the optical properties of actual YSZ samples, Table 2 summarizes the measured transmittance (T) and reflectance (R) at the wavelength of 1028 nm used in this study for the experimental samples. The absorption rate was also calculated using these values and the Eq. 1-T-R. The transmittance of the YSZ substrate increased with increasing dopant from 2 mol% to 5 mol%. This is due to an increase in the ratio of isotropic cubic crystals, which results in higher transmittance of light passing within a single grain and between adjacent grains. In addition, the increase in grain size reduces the number of grain boundaries, which is thought to reduce the effects of intergranular scattering and absorption of incident light. On the other hand, the transmittance of 8Y, which has the highest cubic crystallinity among the four YSZ samples and should theoretically show the highest transmittance, decreased significantly. This could be due to scattering from residual pores in the material identified in Fig. 9 and Fig. 15(d1). During the sintering process of zirconia, some residual pores are entrapped in the process of crystal growth. By controlling the sintering conditions and doing HIP treatment for post-process, residual pores that remain at the grain boundaries can be removed, but intragranular pores cannot be removed. Although some residual pores were also present in 2Y, 3Y, and 5Y, residual pores were very noticeable in 8Y, which may have affected its ablation characteristics.

According to these results, nanofabrication characteristics were considered. Schematics of the difference in laser irradiation behavior of each sample are summarized in Fig. 19. From the experiment, the pore diameter and number of pores increased in the order of 2Y, 3Y, and 5Y, suggesting that the increase in grain size with concentration promotes the lens effect for the pore generation. The larger grains increase the amount of energy that can be focused inside the grain due to the lens

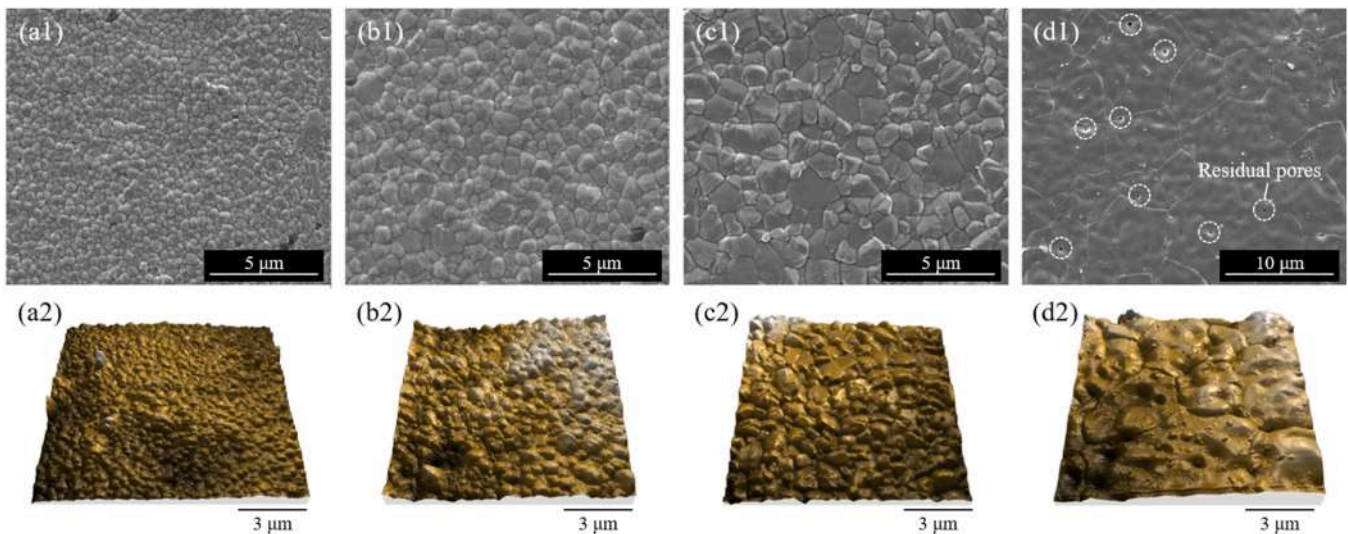


Fig. 15. Surface images of the original YSZ: (a) 2Y, (b) 3Y, (c) 5Y, (d) 8Y. (a1)–(d1) are SEM images, and (a2)–(d2) are three-dimensional topography measured by AFM.

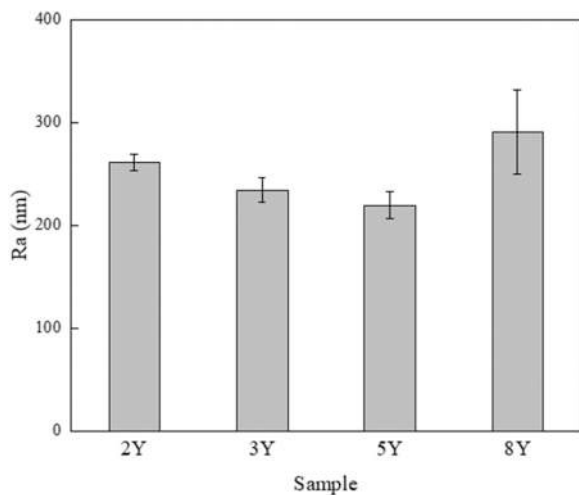


Fig. 16. Surface roughness of original YSZ surface.

effect, which is thought to increase the amount of removed material by ablation within the grains, resulting in a larger number and diameter of pores. In addition, 2Y is more susceptible to the relative increase in the number of grain boundaries due to its smaller grain size, and many intergranular cracks are formed due to localized heat accumulation and thermal stresses at grain boundaries. In 5Y, pores formed preferentially on smaller grains, indicating that pores were more easily formed in the tetragonal grain than in the cubic grain, which is superior in terms of transparency. From this result, it can be said that the effect of the convex shape of the incident beam is more important and dominant for nanopore formation than the optical properties inside the grains. Surface topography after laser irradiation (Fig. 8) also clarified the difference in curvature between the grains with and without pores. This result also shows the effect of surface topography. In addition, the grain boundary can be regarded as a concave shape. Reflected light is concentrated and energy is intensified near the grain boundary, which is also thought to have caused intergranular cracks and processing near the grain boundary.

Intra-grain scattering is also thought to influence pore formation. Scattering occurs at the grain boundaries of 2Y and 3Y, which are composed of anisotropic crystals, and at the boundary between

tetragonal and cubic crystals in 5Y. In addition, a previous study has reported that the refractive index decreases with increasing yttria concentration due to the segregation of dopant, and an increase of a few mol % in yttria concentration decreases the refractive index by about 0.1 [28]. The change in refractive index at grain boundaries in 2Y~5Y with yttria segregation (Fig. 17) is considered to enhance the intragranular scattering and reflection of the incident beam within the grain. Therefore, 2Y, 3Y, and 5Y are more susceptible to internal scattering at grain boundaries, and this scattered/reflected light may act as a supplement to the beam focused by the lens effect on the top surface layer, thereby increasing the local energy inside the grains more and promoting pore formation.

The machined surface of 8Y differed significantly from the other three samples. It was characterized by surface delamination and microcracks at the laser-irradiated area, and the formation of small pores concentrated along grain boundaries. This phenomenon is considered to be due to the thermal diffusivity of the grains, in addition to the local energy absorption from residual pores and defects in the substrate material as a starting point. Bisson et al. [29] showed that the specific heat, thermal diffusivity, and thermal conductivity of YSZ strongly depend on the yttria concentration. Sasaki [30] compared 3Y and 8Y, and found that the thermal diffusivity and conductivity of dense YSZ decreased with increasing concentration. This suggests that thermal accumulation tended to occur near the surface of the 8Y and some 5Y grains in this study, and that cracking was caused by thermal stress, corresponding to the strain concentration near the surface in 8Y (Fig. 9). In addition, the 8Y surface was flatter than the low-concentration sample, and there was less scattering at the grain boundaries, suggesting that larger pores did not form as in the other samples. The small surface pores are thought to be due to energy absorption by intracrystalline defects. It is considered that more pores were formed near the grain boundaries, which are particularly prone to contain defects.

In summary, the phenomenon of nanopore formation in YSZ with different yttria concentrations was mainly affected by grain size and crystal structure. At lower concentrations, the influence of grain boundaries was larger, and surface topography and intragranular reflection due to the crystal structure and dopant segregation within the grains contributed to pore formation. In contrast, these factors were less likely to contribute to pore formation at the higher concentration of 8Y. Based on these results, it is expected that the development of YSZ with precisely controlled grain size and crystal structure will lead to the development of a technique to form more uniform nanopores.

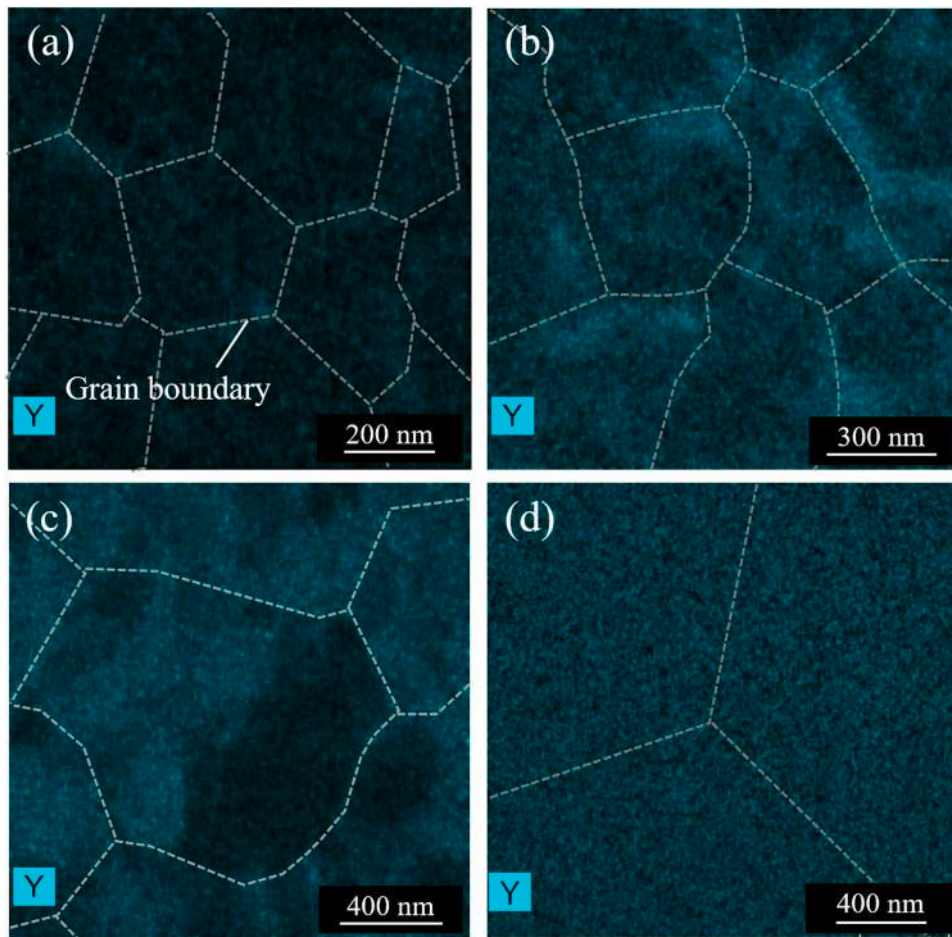


Fig. 17. EDX mapping image of yttrium: (a) 2Y, (b) 3Y, (c) 5Y, (d) 8Y.

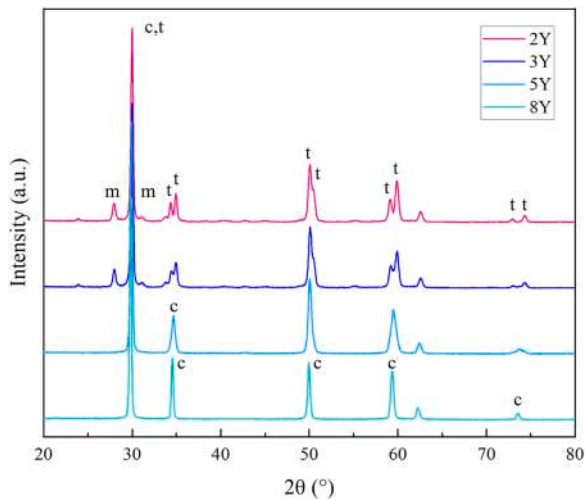


Fig. 18. XRD spectra of the original YSZ surface with different yttria concentrations.

4. Conclusions

Femtosecond pulsed laser irradiation was performed to generate nanopores on YSZ with various dopant concentrations and differences in fundamental processing characteristics were investigated. The conclusions are presented below.

Table 2

Optical property of YSZ at 1028 nm.

Material	T (%)	R (%)	1- T - R (%)
2Y	15.5	67.5	17.0
3Y	23.1	49.7	27.2
5Y	26.5	42.0	31.5
8Y	15.8	68.6	15.6

- (1) In 2Y, 3Y, and 5Y, nanopores of about 100 nm in diameter were uniformly generated in a limited laser power range. The diameter of the nanopores increased with increasing yttria dopant concentration. 2Y had the most intergranular cracks on the surface due to thermal stress. In 5Y, pores formed preferentially on smaller grains. In 8Y, few pores were formed. The region near grain boundaries was preferentially processed, and the surface layer was easily exfoliated and microcracks were generated by increasing laser power.
- (2) Segregation of yttria at grain boundaries slightly increased from 2Y to 3Y; in 5Y, yttria was also spread within the grains, while in 8Y, yttria was uniformly distributed within the material and no segregation occurred. Grain size increased with concentration. As the concentration increased from 2Y to 5Y, the lens effect increased and the intragranular scattering affected the formation of pores. Higher yttria concentration resulted in heat accumulation on the surface of 8Y which induced microcracks.
- (3) 2Y and 3Y consisted of tetragonal and monoclinic phases, 5Y consisted of tetragonal and cubic phases, and 8Y consisted of cubic phases. No thermally induced phase transition was

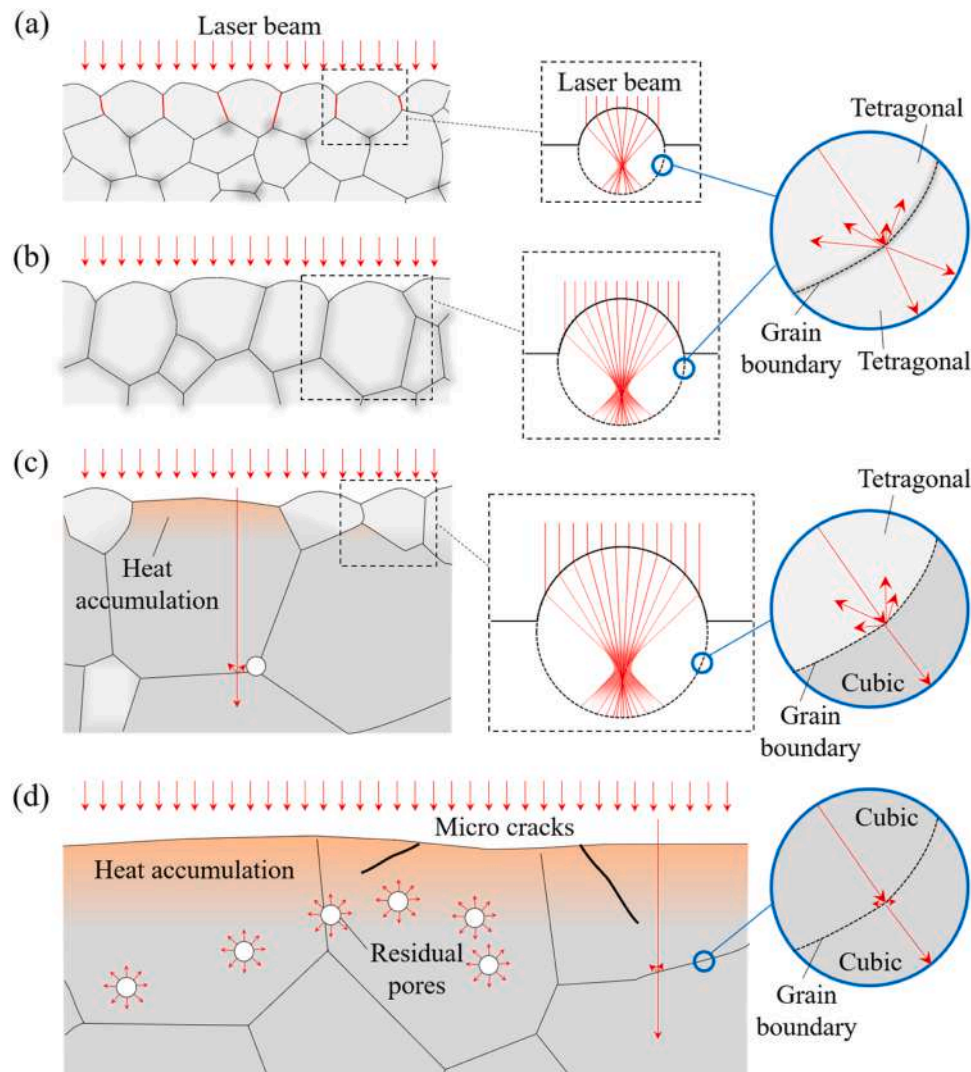


Fig. 19. Difference in laser irradiation behavior: (a) 2Y, (b) 3Y, (c) 5Y, (d) 8Y.

observed after nanopore generation using femtosecond pulses on any irradiated surface, and no damage to the bulk occurred due to thermal effects.

- (4) No significant degradation of material strength due to laser irradiation was observed in 2Y, 3Y, and 5Y with uniformly processed nanopores, and the material strength was maintained.

This study demonstrates the possibility of generating nanopores in the surface layer and functionalizing the surface without causing thermal damage to the bulk, by investigating the nanoscale processing characteristics of femtosecond pulsed laser irradiation of zirconia with different dopant levels. The findings from this study will help to identify suitable materials and processing conditions for nanoscale processing. This will not only deepen the scientific understanding of the interaction between laser and polycrystalline materials, but also offer the possibility to add value to them in various applications by improving surface functionalities such as wettability, biocompatibility, and nanomedicine delivery.

CRediT authorship contribution statement

Yamamuro Yuka: Data curation, Formal analysis, Investigation, Methodology, Validation, Visualization, Writing – original draft, Conceptualization. **Shimoyama Tomotaka:** Conceptualization, Data

curation, Funding acquisition, Investigation, Methodology, Project administration, Resources, Validation. **Nagata Hiroya:** Conceptualization, Data curation, Funding acquisition, Investigation, Methodology, Project administration, Resources, Validation. **Yan Jiwang:** Conceptualization, Funding acquisition, Methodology, Project administration, Resources, Supervision, Writing – review & editing.

Declaration of Competing Interest

The authors declare that they have no known competing financial interests or personal relationships that could have appeared to influence the work reported in this paper.

Data Availability

The raw/processed data required to reproduce these findings cannot be shared at this time due to technical or time limitations.

Acknowledgments

This study has been partially supported by JSPS KAKENHI Grant Number JP22J14123.

References

- [1] R.C. Garvie, R.H. Hannink, R.T. Pascoe, Ceramic steel? *Nature* 258 (1975) 703–704, <https://doi.org/10.1038/258703a0>.
- [2] C. Piconi, G. Maccauro, Zirconia as a ceramic biomaterial, *Biomaterials* 20 (1999) 1–25, [https://doi.org/10.1016/S0142-9612\(98\)00010-6](https://doi.org/10.1016/S0142-9612(98)00010-6).
- [3] B. Feng, Y. Ikuhara, Ionic conductivity in ZrO₂: current status and future perspective, *TOSOH Res. Technol. Rev.* 65 (2021) 17–24.
- [4] L. Yao, J. He, Recent progress in antireflection and self-cleaning technology – from surface engineering to functional surfaces, *Prog. Mater. Sci.* 61 (2014) 94–143, <https://doi.org/10.1016/j.pmatsci.2013.12.003>.
- [5] F. Chen, D. Zhang, Q. Yang, J. Yong, G. Du, J. Si, F. Yun, X. Hou, Bioinspired wetting surface via laser microfabrication, *ACS Appl. Mater. Interfaces* 5 (2013) 6777–6792, <https://doi.org/10.1021/am401677z>.
- [6] M. Omiya, A. Nakajima, J. Yan, Design and fabrication of micro and nano surface structures for enhancing metal–polymer adhesion using femtosecond laser treatment, *Mater. Des.* 224 (2022) 1–11, <https://doi.org/10.1016/j.matdes.2022.111349>.
- [7] M. Kim, S.M. Lee, S.J. Lee, Y.W. Kim, Liang Li, D.W. Lee, Effect on friction reduction of micro/nano hierarchical patterns on sapphire wafers, *Int. J. Precis. Eng. Manuf. - Green. Technol.* 4 (2017) 27–35, <https://doi.org/10.1007/s40684-017-0004-3>.
- [8] L. Salou, A. Hoornaert, J. Stanovici, S. Briand, G. Louarn, P. Layrolle, Comparative bone tissue integration of nanostructured and microroughened dental implants, *Nanomedicine* 10 (2015) 741–751, <https://doi.org/10.2217/nnm.14.223>.
- [9] A.L. Zachman, L.H. Hofmeister, L. Costa, T.C. Boire, Y.S. Hwang, W.H. Hofmeister, H.J. Sung, Femtosecond laser-patterned nanopore arrays for surface-mediated peptide treatment, *Nanomed. Nanotechnol. Biol. Med.* 10 (2014) 11–14, <https://doi.org/10.1016/j.nano.2013.09.002>.
- [10] D. Losic, S. Simovic, Self-ordered nanopore and nanotube platforms for drug delivery applications, *Expert Opin. Drug Deliv.* 6 (2009) 1363–1381, <https://doi.org/10.1517/17425240903300857>.
- [11] T. Kosmač, Č. Oblak, L. Marion, The effects of dental grinding and sandblasting on ageing and fatigue behavior of dental zirconia (Y-TZP) ceramics, *J. Eur. Ceram. Soc.* 28 (2008) 1085–1090, <https://doi.org/10.1016/j.jeurceramsoc.2007.09.013>.
- [12] T.K. Gupta, F.F. Lange, J.H. Bechtold, Effect of stress-induced phase transformation on the properties of polycrystalline zirconia containing metastable tetragonal phase, *J. Mater. Sci.* 13 (1978) 1464–1470, <https://doi.org/10.1007/BF00553200>.
- [13] B. Smielak, L. Klimek, Effect of hydrofluoric acid concentration and etching duration on select surface roughness parameters for zirconia, *J. Prosthet. Dent.* 113 (2015) 596–602, <https://doi.org/10.1016/j.prosdent.2015.01.001>.
- [14] E. Roitero, F. Lasserre, J.J. Roa, M. Anglada, F. Mücklich, E. Jiménez-Piqué, Nanosecond-laser patterning of 3Y-TZP: damage and microstructural changes, *J. Eur. Ceram. Soc.* 37 (2017) 4876–4887, <https://doi.org/10.1016/j.jeurceramsoc.2017.05.052>.
- [15] X. Jing, Z. Pu, S. Zheng, F. Wang, H. Qi, Nanosecond laser induced microstructure features and effects thereof on the wettability in zirconia, *Ceram. Int.* 46 (2020) 24173–24182, <https://doi.org/10.1016/j.ceramint.2020.06.197>.
- [16] R.A. Delgado-Ruiz, J.L. Calvo-Guirado, P. Moreno, J. Guardia, G. Gomez-Moreno, J.E. Mate-Sánchez, P. Ramirez-Fernández, F. Chiva, Femtosecond laser microstructuring of zirconia dental implants, *J. Biomed. Mater. Res. Part B Appl. Biomater.* 96B (2011) 91–100, <https://doi.org/10.1002/jbm.b.31743>.
- [17] A.M. Stanciu, Q. Flamant, C.M. Sprecher, M. Alini, M. Anglada, M. Peroglio, Femtosecond laser multi-patterning of zirconia for screening of cell-surface interactions, *J. Eur. Ceram. Soc.* 38 (2018) 939–948, <https://doi.org/10.1016/j.jeurceramsoc.2017.08.019>.
- [18] Y. Yamamuro, T. Shimoyama, J. Yan, Microscale surface patterning of zirconia by femtosecond pulsed laser irradiation, *Int. J. Precis. Eng. Manuf. Technol.* 9 (2022) 619–632, <https://doi.org/10.1007/s40684-021-00362-3>.
- [19] W. Karim, E. Millon, J. Vulliet, M. Tabbal, A. Thomann, N. Semmar, Applied surface science nano-squares and regular LIPSS on YSZ coating by picosecond UV laser beam: thin film mediated and direct texturing, *Appl. Surf. Sci.* 623 (2023), <https://doi.org/10.1016/j.apsusc.2023.157110>.
- [20] Y. Yamamuro, T. Shimoyama, J. Yan, Generation of nanopore structures in yttria-stabilized zirconia by femtosecond pulsed laser irradiation, *J. Mater. Res. Technol.* 23 (2023) 1155–1176, <https://doi.org/10.1016/j.jmrt.2023.01.079>.
- [21] S. Heiroth, J. Koch, T. Lippert, A. Wokaun, D. Günther, F. Garrelie, M. Guillermin, Laser ablation characteristics of yttria-doped zirconia in the nanosecond and femtosecond regimes, *J. Appl. Phys.* 107 (2010) 014908, <https://doi.org/10.1063/1.3275868>.
- [22] J. Cui, Z. Gong, P. Rao, Effect of molten zone ablated by femtosecond laser on fracture toughness of oxide ceramics, *J. Eur. Ceram. Soc.* 38 (2018) 2440–2444, <https://doi.org/10.1016/j.jeurceramsoc.2017.12.049>.
- [23] T. Yamaguchi, Characterization techniques of ceramic: properties of sintered bodies, *Ceram. Jpn.* 19 (1984) 520–529.
- [24] Y. Cai, W. Chang, X. Luo, Y. Qin, Superhydrophobicity of microstructured surfaces on zirconia by nanosecond pulsed laser, *J. Micro* 2 (2019) 5–14, <https://doi.org/10.1177/2516598418799933>.
- [25] K. Matsui, H. Yoshida, Y. Ikuhara, Grain-boundary structure and microstructure development mechanism in 2–8 mol% yttria-stabilized zirconia polycrystals, *Acta Mater.* 56 (2008) 1315–1325, <https://doi.org/10.1016/j.actamat.2007.11.026>.
- [26] R. Apetz, M.P.B. Van Bruggen, Transparent alumina: a light-scattering model, *J. Am. Ceram. Soc.* 86 (2003) 480–486, <https://doi.org/10.1111/j.1151-2916.2003.tb03325.x>.
- [27] T. Irifune, Synthesis of transparent nano-ceramics under ultra-high pressure, *Rev. High. Press. Sci. Technol. No Kagaku Gijutsu* 28 (2018) 162–169, <https://doi.org/10.4131/jshpreview.28.162>.
- [28] M. Boulouz, L. Martin, A. Boyer, Effect of the dopant content on the physical properties of Y₂O₃-ZrO₂ and CaO-ZrO₂ thin films produced by evaporation and sputtering techniques, *Mater. Sci. Eng. B* 67 (1999) 122–131, [https://doi.org/10.1016/S0921-5107\(99\)00338-4](https://doi.org/10.1016/S0921-5107(99)00338-4).
- [29] J.F. Bisson, D. Fournier, M. Poulain, O. Lavigne, R. Mévrel, Thermal conductivity of yttria-zirconia single crystals, determined with spatially resolved infrared thermography, *J. Am. Ceram. Soc.* 83 (2000) 1993–1998, <https://doi.org/10.1111/j.1151-2916.2000.tb01502.x>.
- [30] Kazuya Sasaki, Influence of defect structure on the thermal conduction characteristic of YSZ polycrystalline, *Netsu Sokutei* 40 (2013) 65–70.